

Grain size in low loss superconducting Ta thin films on c-axis sapphire

Sarah Garcia Jones,^{1,2, a)} Nicholas Materise,^{3, a)} Ka Wun Leung,^{4, a)} Brian D. Isakov,¹ Xi Chen,⁴ Jiangchang Zheng,⁴ András Gyenis,¹ Berthold Jaeck,^{4,5, b)} and Corey Rae H. McRae^{1,2,6, c)}

¹⁾Department of Electrical, Computer, and Energy Engineering, University of Colorado Boulder, Boulder, Colorado 80309, USA

²⁾Department of Physics, University of Colorado, Boulder, Colorado 80309, USA

³⁾Department of Physics, Colorado School of Mines, Golden, Colorado 80401, USA

⁴⁾Department of Physics, The Hong Kong University of Science and Technology, Clear Water Bay, Kowloon, Hong Kong SAR, China

⁵⁾HKUST IAS Center for Quantum Technologies, The Hong Kong University of Science and Technology, Clear Water Bay, Kowloon, Hong Kong SAR, China

⁶⁾National Institute of Standards and Technology, Boulder, Colorado 80305, USA

(Dated: 26 July 2023)

In recent years, the implementation of thin-film Ta has led to improved coherence times in superconducting circuits. Efforts to further optimize this materials set have become a focus of the subfield of materials for superconducting quantum computing. It has been previously hypothesized that grain size could be correlated with device performance. In this work, we perform a comparative grain size experiment with α -Ta on c-axis sapphire. Our evaluation methods include both room-temperature chemical and structural characterization and cryogenic microwave measurements, and we report no statistical difference in device performance between small- and larger-grain-size devices with grain sizes of 924 nm² and 1700 nm², respectively. These findings suggest that grain size is not correlated with loss in the parameter regime of interest for Ta grown on c-axis sapphire, narrowing the parameter space for optimization of this materials set.

I. INTRODUCTION

Superconducting qubits are a promising avenue for scalable quantum computing devices due to their high-fidelity operation^{1–4}. Recent advances in qubit design, packaging, and control have shrunk the gap toward their practical use^{5,6}. Still, dielectric losses due to bulk substrates, surface oxides, and amorphous or defect-ridden material interfaces limit the coherence of superconducting qubits and ancillary devices^{7–9}. Microscopically, materials loss is largely associated with the excitation of two-level systems (TLS) that dominate microwave losses in the technologically relevant range of low temperatures and single-photon numbers^{10,11}. Materials engineering has been identified as a leading route for improvement of superconducting qubit coherence by reducing the effect of TLS¹².

Recent works demonstrate improved qubit performance when α -phase tantalum (Ta) replaces niobium (Nb) as the superconducting thin film base layer for device fabrication^{7,13}. These findings are further supported by loss measurements of superconducting microwave resonators^{8,14–16} and it is believed that the loss reduction is afforded by the simple oxide structure of the Ta film surface⁷. Further evidence for this is suggested by recent work capping Nb films with Ta for improved qubit performance¹⁷.

A detailed materials study of Nb-based qubits links the bulk properties of the polycrystalline films to qubit losses¹⁸. Small crystalline grain sizes were found to correlate with increased

qubit losses, which could arise from TLS present at the sub-surface grain boundary oxides in Nb films¹⁸. Hence, the grain size of the superconducting base layer has recently been debated as a promising process parameter to further minimize microwave losses in Ta films. Moreover, controlled A/B-testing studies would be desirable to firmly establish this relation and it remains unknown whether grain size effects on microwave losses extend to resonators based on Ta films, whose surface and subsurface oxide structure differs from that of Nb films.

The goal of this work is to probe the relationship between grain size and microwave losses for α -Ta films grown on c-axis sapphire, a substrate commonly used for Ta growth^{7,14}. To this end, we perform microwave loss measurements of coplanar waveguide resonators made from magnetron-sputtered α -Ta films with large and small grain sizes. We compare the losses of both types of films across thirty resonators from multiple chips and report no statistical difference between the performance of films with small and larger grain sizes. In combination with results from the chemical and crystallographic thin film characterizations, our observations indicate that grain size does not play a significant role in microwave losses for α -Ta films across the tested parameter regime.

II. TA GROWTH AND CHARACTERIZATION

Ta films of nominal 200 nm thickness were deposited on c-axis sapphire wafers (2" diameter, 550 μ m thickness, from Hefei Keijing Materials Technology) using dc magnetron sputtering. Prior to deposition, the as-purchased substrates were cleaned via ultrasonication in acetone, isopropanol, and deionized water for 5 min each and blown dry with nitrogen

^{a)}These authors contributed equally to this work.

^{b)}bjaeck@ust.hk

^{c)}coreyrae.mcr@colorado.edu

of purity 4N. To deposit thin films with different grain sizes, two different substrate temperatures $T = 400^\circ\text{C}$ (sample label ‘SGS’ or ‘small grain size’) and $T = 500^\circ\text{C}$ (sample label ‘LGS’ or ‘larger grain size’) during the deposition were chosen, while other deposition parameters (background pressure $\leq 1 \times 10^{-7}$ Torr, argon pressure 3 mTorr, deposition power 150 W, deposition rate 3.6 nm/min) were not changed. The deposition was carried out without the use of a seed layer. A $T = 600^\circ\text{C}$ sample was also grown, but no increase in grain size was detected, so this sample is not included in the detailed

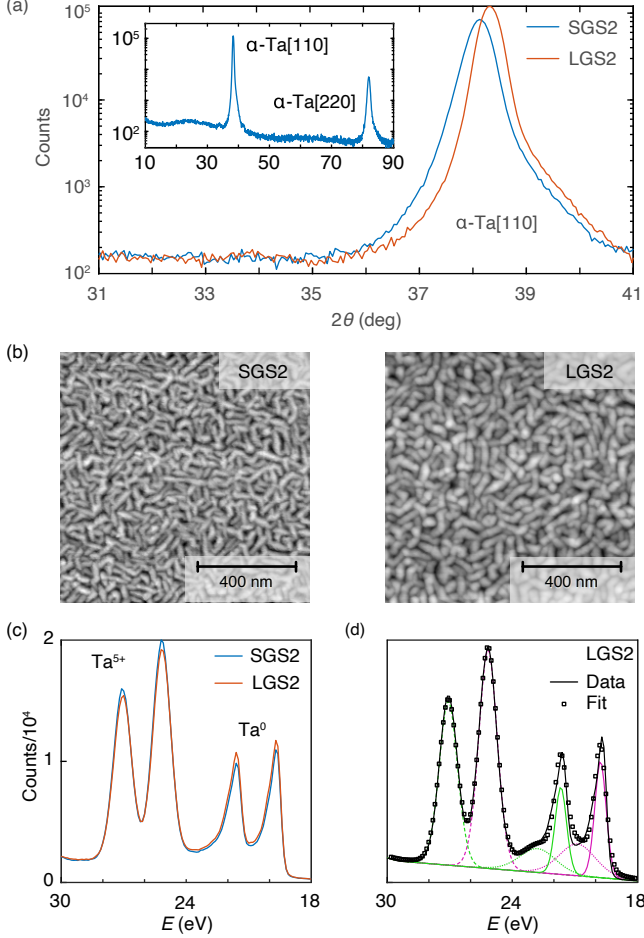


FIG. 1. Structural and chemical characterization of Ta films. (a) X-ray diffraction spectra of 2θ -scans for measurements of the ‘SGS2’ and ‘LGS2’ samples. The inset displays the corresponding spectrum for the ‘LGS2’ sample over a larger angle (θ) range. The detected diffraction peaks are labeled with the corresponding Miller indices of the α -Ta phase. (b) Atomic force microscopy topographies of the ‘SGS2’ (left) and ‘LGS2’ (right) sample surfaces. (c) Electron binding energy spectra of the Ta 4f core level obtained from X-ray photoelectron spectroscopy measurements at the surface of the ‘SGS2’ and ‘LGS2’ samples. The dominant Ta oxidation states are indicated. (d) Least squares fit (open squares) to an XPS spectrum (solid black line) recorded at the surface of the LGS2 sample. Contributions to the spectrum by the Ta 4f_{5/2} (magenta color) and Ta 4f_{7/2} (green color) core levels of Ta, (solid lines), Ta³⁺ (dotted lines), and Ta⁵⁺ (dashed lines) were modeled by using Gaussian profiles.

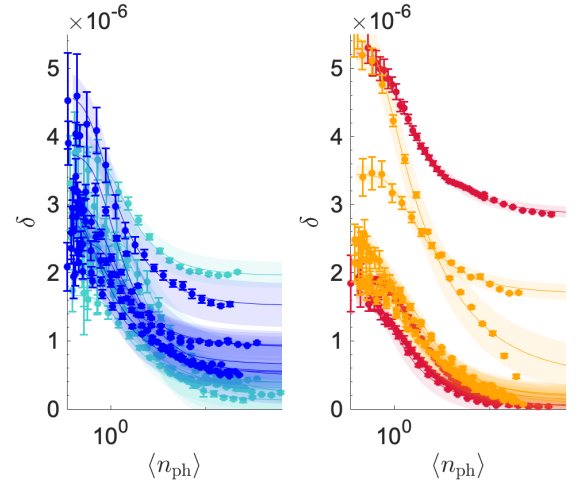


FIG. 2. Resonator loss power curves with small grain size (left) and larger grain size (right). Total loss δ minus high power loss $1/Q_{i,HP}$ as a function of average number of photons in the cavity $\langle n_{ph} \rangle$ for all devices measured in this work - SGS1 (light blue), SGS2 (blue), LGS1 (red), and LGS2 (orange) resonators. Lines denote best fits to the TLS model (Eq. (4)). 95% confidence intervals for Lorentzian fits to each data point are given, as well as the prediction interval for each TLS-curve fit.

film comparison.

The large-scale diffraction spectrum of the films (Fig. 1(a) inset) is dominated by a set of two peaks, which can be associated with diffraction at the [110] and [220] planes of the α -Ta[220] phase. A comparably small diffraction signal, which rises just above the background signal, is detected at $2\theta \approx 33.7^\circ$ that can be associated with the [002]-diffraction of the tantalum β -phase. Our observations indicate the Ta films prepared for this study predominantly nucleate in the α -Ta phase. This finding is consistent with previous reports on 200 nm thick α -Ta films on c -axis sapphire, which were deposited under comparable conditions⁷. The close-up view of the α -Ta[110] peaks for the ‘SGS2’ and ‘LGS2’ samples is shown in the main panel of Fig. 1(a). The diffraction peak of the ‘LGS2’ sample ($\sigma = 0.4^\circ$) has a smaller full-width-half-maximum σ compared to that of the ‘SGS2’ sample ($\sigma = 0.5^\circ$). While this observation is indicative of a larger average grain size in the ‘LGS2’ sample, we note that the Scherrer equation is less suited to quantitatively analyze the grain size in this case, owing to the grain shape anisotropy and significant grain size variations (see AFM measurements below). We further observed a small deviation in the [002]-diffraction angle both between the ‘SGS2’ ($2\theta = 38.1^\circ$) and ‘LGS2’ ($2\theta = 38.3^\circ$) sample, as well as with respect to the nominal bulk value ($2\theta = 38.505^\circ$). This can be attributed to the presence of strain in the thin film structure, which appears slightly more pronounced in the ‘SGS2’ sample.

To characterize the crystalline grain size of the Ta films deposited at different substrate temperatures, we carried out atomic force microscopy (AFM) measurements (tapping mode). The resulting AFM topographies for samples ‘SGS2’ and ‘LGS2’ are shown in Fig. 1(b). Both topographies are

TABLE I. Relative atomic concentration of different tantalum oxidation states in the ‘SGS2’ and ‘LGS2’ samples as obtained from fits to the XPS spectra.

Oxidation state	Small grain size	Larger grain size
	atomic %	atomic %
Ta ⁰	18	20
Ta ³⁺	17	18
Ta ⁵⁺	65	62

characterized by elongated crystalline grains oriented along the hexagonal basal plane of the sapphire surface, consistent with previous reports¹⁴. Moreover, the grains of ‘LGS2’ exhibit a visibly larger grain size area G than those of ‘SGS2’, consistent with our expectations in light of the substrate temperatures during deposition. To quantify these grain size differences, we applied a watershed algorithm¹⁹ to determine G , which is an average across several $1\mu\text{m}^2$ surface areas per sample and several samples for each deposition condition. This approach was previously applied to quantify grain sizes of Nb films¹⁸. We obtain $G = 924 \pm 51\text{nm}^2$ for the ‘SGS2’ and $G = 1700 \pm 29\text{nm}^2$ for the ‘LGS2’ sample, respectively. Interestingly, the average grain size $G = 1732 \pm 92\text{nm}^2$ of samples deposited at a substrate temperature $T = 600^\circ\text{C}$ is comparable to that of the $T = 500^\circ\text{C}$ deposition²⁰.

To detect the possible influence of the crystalline grain size on the surface oxide structure, we performed X-ray photoelectron spectroscopy (XPS) measurements (Kraxis Ultra DLD; X-ray source: Al $K\alpha$ line $E = 1486.6\text{eV}$) on the ‘SGS2’ and ‘LGS2’ samples. We note that these samples did not undergo surface treatment to remove native surface oxides prior to XPS measurements. The resulting XPS spectra in Fig. 1(c) show the photo-electron count as a function of the electron binding energy for the Ta-4f core level. The spectra are dominated by a four peak structure, which is predominantly composed of the spin-orbit split Ta⁰ and Ta⁵⁺ doublets that can be assigned to the metallic Ta bulk and the Ta₂O₅ at the film surface, respectively^{21,22}.

We quantify the relative contributions of the different Ta oxidation states to the observed XPS spectra by applying a least-squares fit based on Gaussian profiles. We find a three doublet structure composed of six Gaussians, as shown in Fig. 1(d), can most accurately describe these spectra. The additional third doublet exhibits a core level shift of $\approx 1.1\text{eV}$ and can be assigned to the Ta³⁺ oxidation state of the Ta₂O₃ suboxide²². The resulting relative contributions of Ta, Ta³⁺, and Ta⁵⁺ obtained from these fits are shown in Table I and reveal a near identical chemical structure of the tantalum film surface for both samples. This is consistent with their almost identical XPS spectra (cf. Fig. 1(c)). The relative spectral weight of the Ta⁰ and Ta⁵⁺ peaks at the given incident X-ray energy is in close agreement with that found in previous XPS studies of tantalum films and indicates a surface oxide thickness of approximately 2nm ⁷.

III. DEVICE DESIGN AND FABRICATION

All devices are coplanar waveguide resonators fabricated using the same designs as reported by Kopas *et al.*²³. Nominally identical designs and fabrication procedures were used for all samples. Prior to etching, the samples were cleaned via ultrasonication in toluene, acetone, methanol, and isopropanol, then patterned using optical lithography and AZ-P4330-RS photoresist. The films were etched in a single 4 minute CF₄/N₂ Inductively Coupled Plasma – Reactive Ion Etch (Panasonic E640). Since the Ta films were deposited on sapphire substrates, the etches did not produce any trenching into the substrate. After etching, the resist was submerged in AZ 300 T stripper at 80°C for 1 hour. After stripping, the samples were diced and again cleaned ultrasonically in toluene, acetone, methanol, and isopropanol before being wire bonded for cryogenic microwave measurement. Optical images of the resonators are shown in Fig. 3.

Inverse coupling quality factors, $1/Q_c$, of the fabricated resonators are presented in Supplementary Materials Table 1 and range from 1.18×10^{-6} to 6.61×10^{-6} across all devices. This is a larger spread of values with a trend towards smaller coupling factors than the simulated $1/Q_c$ values of these designs, which ranged from 1.95×10^{-6} to 2.02×10^{-6} .²³ This variation is likely due to a slight over etch of the devices during fabrication, which is congruent with a thinner measured conductor width than the lithography designs used (design: $6\mu\text{m}$, measured: $5.5\mu\text{m}$).

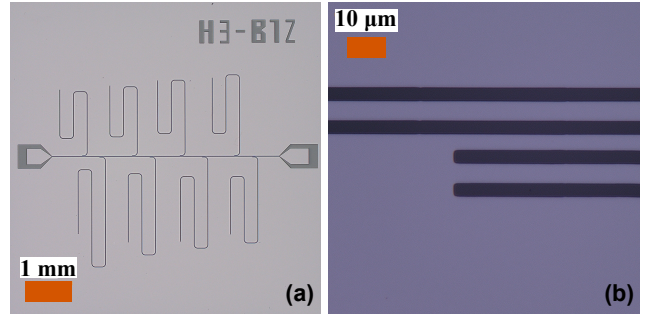


FIG. 3. Optical microscope images of coplanar waveguide resonators. (a) Full chip image of a representative chip. All circuits measured contain eight resonators with identical couplers. (b) Close up of feedline and resonator base. Conductor width is $5.5\mu\text{m}$ and gap is $3.8\mu\text{m}$.

IV. CRYOGENIC MICROWAVE MEASUREMENT

We perform transmission measurements on CPW resonators mounted to the mixing chamber (MXC) plate of a FormFactor (formerly Janis) JDry 250 dilution refrigerator (DR) at a mixing chamber temperature of $\sim 10\text{mK}$ using a Keysight PNA N5222B vector network analyzer (VNA). The input power varied over ten orders of magnitude in estimated photon power to accurately extract the dominant two level system (TLS) loss²⁴.

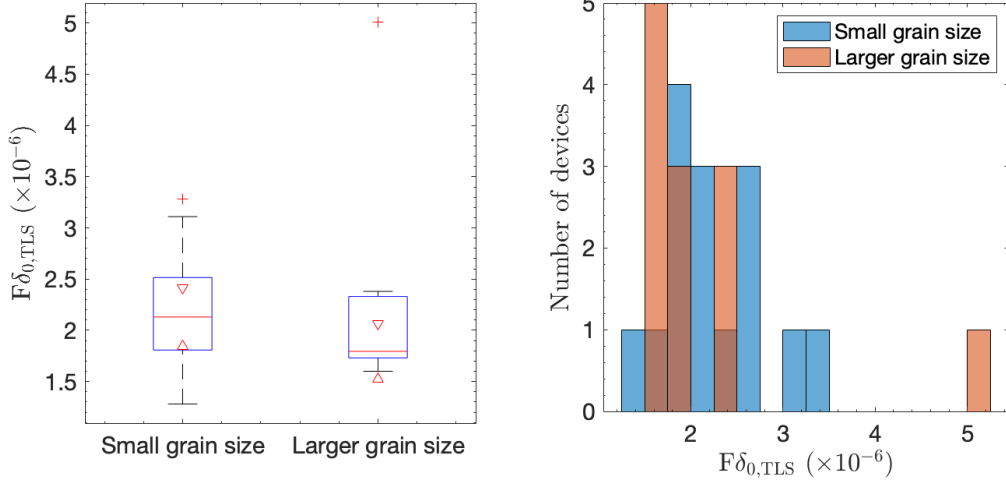


FIG. 4. TLS loss in Ta on c-axis sapphire superconducting microwave resonators with small and larger grain size. Left: Box and whiskers comparison, indicating median values (red line) and 95% confidence interval of median (red triangles), with outliers shown as crosses. Right: Histogram of TLS loss for all devices in this experiment.

Nominally identical gold-plated oxygen-free high conductivity copper sample boxes house the resonator chips and are mounted to a plate perpendicular to the MXC plate with additional mu-metal shielding surrounding all samples. Two Radi-all R583 six-way microwave switches allow multiple samples to be measured on the same pair of coaxial input and output lines.

The transmission data for each resonator (S_{21} of the two-port S -parameter matrix measured by the VNA) is first normalized with a circle fit²⁵, and then fit to a diameter-corrected asymmetric Lorentzian model of the form²⁶,

$$S_{21}(f) = 1 - \frac{Q_l / Q_c e^{i\phi}}{1 + 2iQ \frac{f-f_0}{f_0}} \quad (1)$$

$$Q_i^{-1} = Q_l^{-1} - \text{Re} \{ \hat{Q}_c^{-1} \} \quad (2)$$

$$\hat{Q}_c^{-1} = Q_c^{-1} e^{i\phi} \quad (3)$$

where f_0 is the resonance frequency, ϕ is the asymmetry angle, Q_c is coupling quality factor, Q_l is the loaded quality factor, and Q_i is the internal quality factor. These parameters are fit with their corresponding 95% confidence intervals from a least squares fitting routine²⁷. A secondary fit of the loss $\delta = Q_i^{-1}$ as a function of average number of photons $\langle n_{ph} \rangle$ and fixed temperature T follows from the sum of the TLS loss contribution δ_{TLS} and an offset term $1/Q_{HP}$ that accounts for power-independent losses dominating at higher powers¹¹

$$\delta(\langle n_{ph} \rangle, T) = \delta_{TLS}(\langle n_{ph} \rangle, T) + 1/Q_{HP} \quad (4)$$

$$\delta_{TLS}(\langle n_{ph} \rangle, T) = F\delta_{TLS}^0 \frac{\tanh\left(\frac{\hbar\omega_0}{k_B T}\right)}{\left(1 + \frac{\langle n_{ph} \rangle}{n_c}\right)^\beta} \quad (5)$$

where n_c is the critical photon number at which TLS saturate at low power, $\omega_0 = 2\pi f_0$ is the angular resonance frequency, β

TABLE II. Mean parameter values in A/B grain size comparison.

	Small grain size	Large grain size
Grain area (nm ²)	924 ± 51	1700 ± 29
$F\delta_{TLS}^0$ (×10 ⁻⁶)	2.19 ± 0.07	2.17 ± 0.03

is an exponent interpolating between the non-interacting TLS model $\beta = 1/2$ and interacting TLS model $\beta < 1/2$ ^{24,28,29}, δ_{TLS}^0 is the intrinsic TLS loss, F is the geometry-dependent filling factor, \hbar is the reduced Planck constant, and k_B is the Boltzmann constant.

In Fig. 2, we plot the loss power dependence for all large and small grain size devices used in this work. The high power losses are subtracted to emphasize the similar power dependence (line shape) and low power loss (TLS saturation loss) between the two samples, without the confounding factor of high-power losses which are known to be caused by a myriad of sources external to the device materials¹¹. Figure 4 further highlights this point, as the medians from the box and whisker plots of the intrinsic TLS losses for the large and small grain size Ta films coincide with one another and their respective histograms give similar variances.

V. LITERATURE COMPARISON

Mean parameter values for the two resonator populations are summarized in Tab. II. Though our small-geometry resonators are very sensitive to TLS loss, we see no statistical difference in TLS loss between the small-grain and large-grain devices, despite the difference in grain size (with the large grain size devices being almost twice as big in area). This difference in grain size is similar to that seen in Nb films in Ref.¹⁸, where a difference in grain size of a factor of two was

correlated with a difference in qubit T_1 of almost two, and a difference in resonator TLS loss was also detected.

We refer to recent studies, especially the work by Lozano *et al.*¹⁶, to estimate the number of devices required to adequately sample the device-to-device variation in $F\delta_{\text{TLS}}^0$. With more than ten devices of each grain size, we exceed the number of devices for each variation (choice of control parameter value) in Refs. Crowley *et al.*⁸, Alegria *et al.*¹⁴, Lozano *et al.*¹⁶, Jia *et al.*³⁰.

The median values of the losses for the untreated Ta resonators on silicon in Ref. Lozano *et al.*¹⁶ are comparable to the large- and small-grain size median losses reported in Fig. 4(a).

Figure 5 shows that the difference between the large- and small-grain size losses in this study is imperceptible on the same scale as other A/B comparisons, e.g. Refs. Alegria *et al.*¹⁴, Lozano *et al.*¹⁶

VI. DISCUSSION

An enduring hypothesis in the superconducting qubit community has been that larger grain size in superconducting thin films is an indication of improved device performance. The simple and stable oxide structure of Ta differs from that of Nb, where Premkumar *et al.*¹⁸ reported that smaller grain size films exhibited higher concentrations of suboxides in interface regions, resulting in measurably higher losses in their Nb resonators. In this study, we show that smaller grain size does not induce significant low power loss in Ta thin films grown between 400 and 500 °C on *c*-axis sapphire.

Microwave measurements of low power loss suggest that there is no statistically significant difference between the intrinsic TLS losses of the two grain size Ta thin films. Chemical and structural analysis support this interpretation, as the surface chemistry obtained by XPS is nearly identical for the two films. This distinguishes densely packed Ta films with their simple Ta₂O₅ surface oxide structure⁷ from Nb films¹⁸ for which subsurface grain boundary oxides contribute a grain size dependent TLS channel. Following this train of thought, we expect qubits and resonators fabricated from Ta films to exhibit more uniform microwave losses than those fabricated from Nb. At the same time, non-negligible concentrations of Ta³⁺ species found in our XPS measurements indicates the presence of Ta₂O₃ suboxides at the Ta metal-Ta₂O₅ interface consistent with a recent report³¹. Interestingly, we also detect practical limits within which to tune the grain size of [110]-oriented α -Ta films deposited on *c*-axis sapphire: Deposition at substrate temperatures below 400 °C favors the formation of the unwanted β -phase^{32,33} whereas grain size does not respond to an increase of substrate temperature in excess of 500 °C in our study. Thus, it would be interesting to explore other substrates or sapphire surface orientations to promote larger grain sizes up to the formation of single-crystalline Ta films. On the other hand, our study suggests more sophisticated materials engineering efforts that focus on the reduction of TLS losses at the immediate metal-air surface rather than on the optimization of bulk properties, such as grain size, are required to further reduce microwave losses below those reported in this and other recent studies^{14,16}. These efforts will benefit from targeted A/B testing studies, such as is presented here, to address the vast materials and processing parameter space in order to maximize state-of-the-art superconducting qubit performance.

VII. CONCLUSION

We performed millikelvin microwave transmission measurements of α -phase Ta microwave resonators with both large- and small-grain size sputter-deposited on *c*-axis sapphire at two different growth temperatures. Structural and chemical analysis reveal that the films differ only in their grain size and not in their surface oxide types and concentrations, and crystal structure. The extracted intrinsic TLS losses show no statistical difference between the two film types, suggesting that, in this materials regime, grain size does not significantly affect millikelvin, ultralow power dielectric loss. We encourage future A/B experimentation to continue to reduce the fabrication parameter space and to identify correlations between other room-temperature materials characterization parameters and low-power, low-temperature microwave performance of devices.

ACKNOWLEDGMENTS

The authors would like to thank Qiming Shao and Jiacheng Liu for their assistance with the sputter deposition, and Carlos

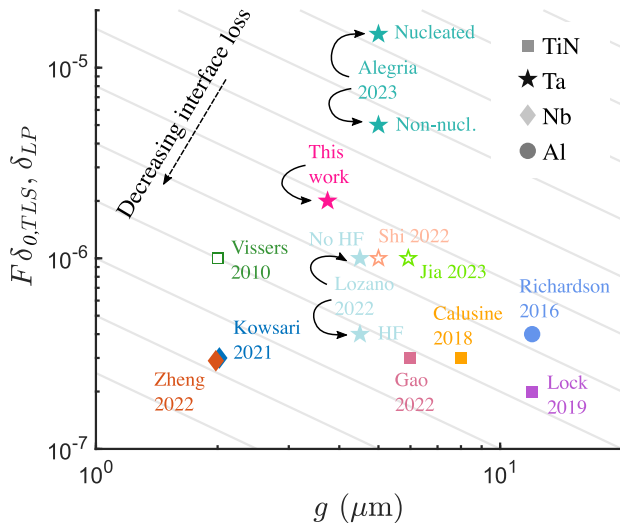


FIG. 5. State-of-the-art literature comparison of TLS ($F\delta_{\text{TLS}}^0$) and low-power (δ_{LP}) loss values in CPW resonators. Filling factor F is estimated by plotting loss as a function of CPW gap width g . Grey lines denote lines of constant interface loss. Filled symbols denote TLS loss values, while empty symbols represent low power loss (TLS loss values unavailable).

Torres Castanedo, David Garcia, Tony McFadden, and Dominic Goronzy for helpful discussions and feedback on the manuscript. N.M. acknowledges funding from the Graduate Fellowships for STEM Diversity. B.J. acknowledges funding from the Croucher Foundation.

AUTHOR DECLARATIONS

Conflicts of Interest

The authors have no conflicts of interest.

Commercial Products Disclaimer

Certain commercial instruments are identified to specify the experimental study adequately. This does not imply endorsement by NIST or that the instruments are the best available for the purpose.

Author Contributions

Sarah Garcia Jones: Resonator sample fabrication (lead), Writing - review & editing; **Nicholas Materise:** Writing - original draft (lead), Writing - review & editing (supporting), Data acquisition (equal), Software (equal); **Ka Wun Leung:** Materials fabrication (lead); **Brian D. Isakov:** Writing - review & editing; **Chen Xi:** Materials characterization (lead); **András Gyenis:** Writing - review & editing, Resonator sample fabrication; **Bertold Jaeck:** Conceptualization (equal), Writing - review & editing (lead), Visualization (equal), Formal analysis (equal), Methodology (lead); **Corey Rae H. McRae:** Conceptualization (equal), Writing - review & editing (lead), Visualization (equal), Formal analysis (equal), Methodology (lead).

DATA AVAILABILITY

The data that support the findings of this study are openly available at <https://zenodo.org/record/8161535>, reference number 10.5281/zenodo.8161535.

REFERENCES

- M. Kjaergaard, M. E. Schwartz, J. Braumüller, P. Krantz, J. I.-J. Wang, S. Gustavsson, and W. D. Oliver, “Superconducting Qubits: Current State of Play,” *Annual Review of Condensed Matter Physics* **11**, 369–395 (2020).
- H. Zhang, S. Chakram, T. Roy, N. Earnest, Y. Lu, Z. Huang, D. K. Weiss, J. Koch, and D. I. Schuster, “Universal fast-flux control of a coherent, low-frequency qubit,” *Phys. Rev. X* **11**, 011010 (2021).
- E. Hyppä, S. Kundu, C. F. Chan, A. Gunyhó, J. Hotari, D. Janzso, K. Juliusson, O. Kiuru, J. Kotilahti, A. Landra, W. Liu, F. Marxer, A. Mäkinen, J.-L. Orgiazzi, M. Palma, M. Savitskyi, F. Tosto, J. Tuorila, V. Vadimov, T. Li, C. Ockeloen-Korppi, J. Heinsoo, K. Y. Tan, J. Hassel, and M. Möttönen, “Unimon qubit,” *Nature Communications* **13**, 6895 (2022).
- J. Howard, A. Lidiak, C. Jameson, B. Basyildiz, K. Clark, T. Zhao, M. Bal, J. Long, D. P. Pappas, M. Singh, and Z. Gong, “Demonstrating two-qubit entangling gates at the quantum speed limit using superconducting qubits,” *arXiv e-prints*, [arXiv:2206.07716](https://arxiv.org/abs/2206.07716) (2022), [arXiv:2206.07716 \[quant-ph\]](https://arxiv.org/abs/2206.07716).
- J. Preskill, “Quantum computing in the nisy era and beyond,” *Quantum* **2**, 79 (2018).
- F. Arute, K. Arya, R. Babbush, D. Bacon, J. C. Bardin, R. Barends, R. Biswas, S. Boixo, F. G. Brandao, D. A. Buell, *et al.*, “Quantum supremacy using a programmable superconducting processor,” *Nature* **574**, 505–510 (2019).
- A. P. M. Place, L. V. H. Rodgers, P. Mundada, B. M. Smitham, M. Fitzpatrick, Z. Leng, A. Premkumar, J. Bryon, A. Vrajitoarea, S. Sussman, G. Cheng, T. Madhavan, H. K. Babla, X. H. Le, Y. Gang, B. Jäck, A. Gye-nis, N. Yao, R. J. Cava, N. P. de Leon, and A. A. Houck, “New material platform for superconducting transmon qubits with coherence times exceeding 0.3 milliseconds,” *Nature Communications* **12**, 1779 (2021).
- K. D. Crowley, R. A. McLellan, A. Dutta, N. Shumiyi, A. P. M. Place, X. Hoang Le, Y. Gang, T. Madhavan, N. Khedkar, Y. Cady Feng, E. A. Umbarkar, X. Gui, L. V. H. Rodgers, Y. Jia, M. M. Feldman, S. A. Lyon, M. Liu, R. J. Cava, A. A. Houck, and N. P. de Leon, “Disentangling Losses in Tantalum Superconducting Circuits,” *arXiv e-prints*, [arXiv:2301.07848](https://arxiv.org/abs/2301.07848) (2023), [arXiv:2301.07848 \[quant-ph\]](https://arxiv.org/abs/2301.07848).
- A. P. Read, B. J. Chapman, C. U. Lei, J. C. Curtis, S. Ganjam, L. Krayzman, L. Frunzio, and R. J. Schoelkopf, “Precision measurement of the microwave dielectric loss of sapphire in the quantum regime with parts-per-billion sensitivity,” *arXiv e-prints*, [arXiv:2206.14334](https://arxiv.org/abs/2206.14334) (2022), [arXiv:2206.14334 \[quant-ph\]](https://arxiv.org/abs/2206.14334).
- C. Müller, J. H. Cole, and J. Lisenfeld, “Towards understanding two-level-systems in amorphous solids: insights from quantum circuits,” *Rep. Prog. Phys.* **82**, 124501 (2019).
- C. R. H. McRae, H. Wang, J. Gao, M. R. Vissers, T. Brecht, A. Dunsworth, D. P. Pappas, and J. Mutus, “Materials loss measurements using superconducting microwave resonators,” *Review of Scientific Instruments* **91** (2020), [10.1063/5.0017378](https://doi.org/10.1063/5.0017378), 091101, https://pubs.aip.org/aip/rsi/article-pdf/doi/10.1063/5.0017378/14797873/091101_1_online.pdf.
- I. Siddiqi, “Engineering high-coherence superconducting qubits,” *Nature Reviews Materials* **6**, 875–891 (2021).
- C. Wang, X. Li, H. Xu, Z. Li, J. Wang, Z. Yang, Z. Mi, X. Liang, T. Su, C. Yang, G. Wang, W. Wang, Y. Li, M. Chen, C. Li, K. Linghu, J. Han, Y. Zhang, Y. Feng, Y. Song, T. Ma, J. Zhang, R. Wang, P. Zhao, W. Liu, G. Xue, Y. Jin, and H. Yu, “Towards practical quantum computers: transmon qubit with a lifetime approaching 0.5 milliseconds,” *npj Quantum Information* **8**, 3 (2022).
- L. Alegria, D. M. Tennant, K. R. Chaves, J. R. I. Lee, S. R. O’Kelley, Y. J. Rosen, and J. L. DuBois, “Two-Level Systems in Nucleated and Non-Nucleated Epitaxial alpha-Tantalum films,” *arXiv e-prints*, [arXiv:2301.10306](https://arxiv.org/abs/2301.10306) (2023), [arXiv:2301.10306 \[cond-mat.supr-con\]](https://arxiv.org/abs/2301.10306).
- L. Shi, T. Guo, R. Su, T. Chi, Y. Sheng, J. Jiang, C. Cao, J. Wu, X. Tu, G. Sun, J. Chen, and P. Wu, “Tantalum microwave resonators with ultrahigh intrinsic quality factors,” *Applied Physics Letters* **121**, 242601 (2022), <https://doi.org/10.1063/5.0124821>.
- D. P. Lozano, M. Mongillo, X. Piao, S. Couet, D. Wan, Y. Canvel, A. M. Vadiraj, T. Ivanov, J. Verjauw, R. Acharya, J. Van Damme, F. A. Mohiyaddin, J. Jussot, P. P. Gowda, A. Pocco, B. Raes, J. Van de Vondel, I. P. Radu, B. Govoreanu, J. Swerts, A. Potočník, and K. De Greve, “Manufacturing high-Q superconducting α -tantalum resonators on silicon wafers,” *arXiv e-prints*, [arXiv:2211.16437](https://arxiv.org/abs/2211.16437) (2022), [arXiv:2211.16437 \[quant-ph\]](https://arxiv.org/abs/2211.16437).
- M. Bal, A. A. Murthy, S. Zhu, F. Crisa, X. You, Z. Huang, T. Roy, J. Lee, D. van Zanten, R. Pilipenko, I. Nekrashevich, D. Bafia, Y. Krasnikova, C. J. Kopas, E. O. Lachman, D. Miller, J. Y. Mutus, M. J. Reagor, H. Cansizoglu, J. Marshall, D. P. Pappas, K. Vu, K. Yadavalli, J.-S. Oh, L. Zhou, M. J. Kramer, F. Q. Lecocq, D. P. Goronzy, C. G. Torres-Castanedo, G. Pritchard, V. P. Dravid, J. M. Rondinelli, M. J. Bedzyk, M. C. Hersam, J. Zasadzinski, J. Koch, J. A. Sauls, A. Romanenko, and A. Grassellino, “Systematic improvements in transmon qubit coherence enabled by niobium surface encapsulation,” (2023), [arXiv:2304.13257 \[cond-mat, physics:quant-ph\]](https://arxiv.org/abs/2304.13257).
- A. Premkumar, C. Weiland, S. Hwang, B. Jäck, A. P. Place, I. Waluyo, A. Hunt, V. Bisogni, J. Pellicciari, A. Barbour, *et al.*, “Microscopic relaxation channels in materials for superconducting qubits,” *Communications Materials* **2**, 72 (2021).

- ¹⁹A. Rabbani and S. Ayatollahi, “Comparing three image processing algorithms to estimate the grain-size distribution of porous rocks from binary 2d images and sensitivity analysis of the grain overlapping degree,” *Special Topics & Reviews in Porous Media: An International Journal* **6** (2015).
- ²⁰“see supplementary information of this manuscript.”
- ²¹G. McGuire, G. K. Schweitzer, and T. A. Carlson, “Core electron binding energies in some group iiia, vb, and vib compounds,” *Inorganic Chemistry* **12**, 2450–2453 (1973).
- ²²F. Himpsel, J. Morar, F. McFeely, R. Pollak, and G. Hollinger, “Core-level shifts and oxidation states of ta and w: Electron spectroscopy for chemical analysis applied to surfaces,” *Physical Review B* **30**, 7236 (1984).
- ²³C. J. Kopas, E. Lachman, C. R. H. McRae, Y. Mohan, J. Y. Mutus, A. Nersisyan, and A. Poudel, “Simple coplanar waveguide resonator mask targeting metal-substrate interface,” *arXiv e-prints*, [arXiv:2204.07202](https://arxiv.org/abs/2204.07202) (2022), [arXiv:2204.07202 \[quant-ph\]](https://arxiv.org/abs/2204.07202).
- ²⁴J. Gao, *The physics of superconducting microwave resonators*, Ph.D. thesis, California Institute of Technology (2008).
- ²⁵S. Probst, F. Song, P. Bushev, A. Ustinov, and M. Weides, “Efficient and robust analysis of complex scattering data under noise in microwave resonators,” *Rev. Sci. Instrum.* **86**, 024706 (2015).
- ²⁶M. Khalil, M. Stoutimore, F. Wellstood, and K. Osborn, “An analysis method for asymmetric resonator transmission applied to superconducting devices,” *J. Appl. Phys.* **111**, 054510 (2012).
- ²⁷(2023), see <https://github.com/Boulder-Cryogenic-Quantum-Testbed/> for data acquisition, preprocessing, and data fitting software used in this work.
- ²⁸W. A. Phillips, “Tunneling states in amorphous solids,” *Journal of Low Temperature Physics* **7**, 351–360 (1972).
- ²⁹S. De Graaf, L. Faoro, J. Burnett, A. Adamyan, A. Y. Tzalenchuk, S. Kubatkin, T. Lindström, and A. Danilov, “Suppression of low-frequency charge noise in superconducting resonators by surface spin desorption,” *Nat. Commun.* **9**, 1–6 (2018).
- ³⁰H. Jia, B. Zhou, T. Wang, Y. Wu, I. Yang, Z. Ding, S. Li, K. Xiong, and J. Feng, “ α -tantalum (110) films grown on a-plane sapphire substrate by molecular beam epitaxy for low-loss superconducting coplanar waveguide resonators,” (2023), [arXiv:2306.09566 \[cond-mat, physics:physics\]](https://arxiv.org/abs/2306.09566).
- ³¹R. A. McLellan, A. Dutta, C. Zhou, Y. Jia, C. Weiland, X. Gui, A. P. M. Place, K. D. Crowley, X. Hoang Le, T. Madhavan, Y. Gang, L. Baker, A. R. Head, I. Waluyo, R. Li, K. Kisslinger, A. Hunt, I. Jarrige, S. A. Lyon, A. M. Barbour, R. J. Cava, A. A. Houck, S. L. Hulbert, M. Liu, A. L. Walter, and N. P. de Leon, “Chemical profiles of the oxides on tantalum in state of the art superconducting circuits,” *arXiv e-prints*, [arXiv:2301.04567](https://arxiv.org/abs/2301.04567) (2023), [arXiv:2301.04567 \[cond-mat.mtrl-sci\]](https://arxiv.org/abs/2301.04567).
- ³²R. Knepper, B. Stevens, and S. P. Baker, “Effect of oxygen on the thermomechanical behavior of tantalum thin films during the β – α phase transformation,” *Journal of applied physics* **100**, 123508 (2006).
- ³³S. Myers, J. Lin, R. M. Souza, W. D. Sproul, and J. J. Moore, “The β to α phase transition of tantalum coatings deposited by modulated pulsed power magnetron sputtering,” *Surface and Coatings Technology* **214**, 38–45 (2013).